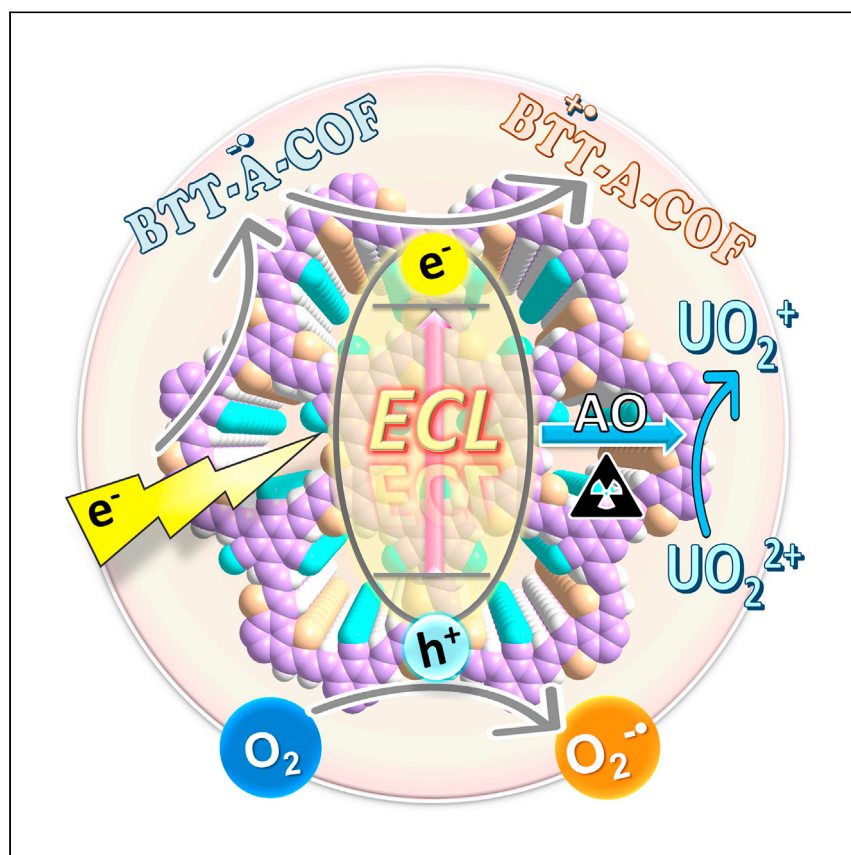**Article**

Tunable covalent organic framework electrochemiluminescence from non-electroluminescent monomers

Electrochemiluminescence research is somewhat limited to a few compounds. Cui et al. report a tunable electrochemiluminescence luminophore family of covalent organic frameworks with high efficiency from non-emitting molecules and their application in uranyl ion detection.

Wei-Rong Cui, Ya-Jie Li, Qiao-Qiao Jiang, ..., Li Zhang, Juewen Liu, Jian-Ding Qiu

jdqiu@ncu.edu.cn

Highlights

Tunable ECL luminophores of COF from non-emitting monomers

ECL can be regulated by changing the electron-withdrawing monomer

Poisonous exogenous co-reactants are not required

Highly selective analysis of uranyl ion is realized

Cell Reports
Physical Science

Article

Tunable covalent organic framework electrochemiluminescence from non-electroluminescent monomers

Wei-Rong Cui,[1,3] Ya-Jie Li,[1,3] Qiao-Qiao Jiang,[1] Qiong Wu,[1] Ru-Ping Liang,[1] Qiu-Xia Luo,[1] Li Zhang,[1] Juewen Liu,[2] and Jian-Ding Qiu[1,4,*]

SUMMARY

It is hard to find new electrochemiluminescence (ECL) luminophores using existing research strategies, especially from ECL non-active monomers. Here, fully conjugated covalent organic frameworks with trithiophene (BTT-COFs) are found to have ultra-high ECL efficiencies (up to 62.2%), even in water and without exogenous co-reactants. Quantum chemistry calculations confirm that the periodic BTT-COFs arrays promote intramolecular electron transfer generating ECL from non-ECL monomers. Modulation of ECL performance is possible by substituting the monomers for those with different electron-withdrawing properties. In addition, the cyano group weaved in the skeleton provides the dense sites for post-functionalization. As a typical use case, a highly selective ECL probe for uranyl ions is reported. The tunable ECL luminophore family possesses a broader development space than the traditional emitters, demonstrates the prospects of ECL-COFs, and affords an idea for detecting various contaminants through the rational design of target ligands.

INTRODUCTION

Electrochemiluminescence (ECL), as a cutting-edge analytical technology, is more selective and sensitive than other optical methods because the generation of excited states can be controlled by changing the electrode potential and there is no interference from scattered light.[1–3] The reported aqueous ECL emitters can be divided into two categories: traditional inorganic molecules and organic aggregation-induced electrochemiluminescence (AIECL) molecules.[4] Among them, the inorganic luminophores (e.g., $[Ru(bpy)_3]^{2+}$, $Ir(ppy)_3$) possess higher quantum yields, but the post-modification capability is quite limited.[1] Alternative organic AIECL-gens (e.g., tetraphenylethene,[5–7] siloles,[8,9] pyrrole,[10] and their derivatives) are metal free and have excellent fine-tuning attributes, emerging as an innovative route for ECL in aqueous solution. However, the research of AIECL is limited to the few compounds above, their aggregation is realized by restricting molecular rotation in poor solvents, and the products are random and disordered.[4] It is hard to broaden the vision to construct a luminophore family by regulating the structure, composition, or spatial orientation for growing detection needs. Most luminophores based on the co-reaction mechanism rely on the high-active co-reactants represented by $S_2O_8^{2-}$ and tripropylamine (TPA) to provide stable free radical ions. Although ECL signals are obtained, the corrosiveness and biotoxicity of these co-reactants do not conform to the pursuit of "green" and "environmentally friendly."[7,11] In addition, the undesirable interference caused by the additional exogenous co-reactants may occur in the accurate detection of trace targets.

[1]College of Chemistry, Nanchang University, Nanchang 330031, China

[2]Department of Chemistry, Waterloo Institute for Nanotechnology, University of Waterloo, ON N2L 3G1, Canada

[3]These authors contributed equally

[4]Lead contact

*Correspondence: jdqiu@ncu.edu.cn

https://doi.org/10.1016/j.xcrp.2021.100630

Cell Reports
Physical Science
Article

The development of covalent organic frameworks (COFs) may bring an unprecedented opportunity for the development of ECL sensors. As burgeoning molecular crystal materials, COFs allow the organic building blocks to assemble into the extended conjugate skeletons, achieving the overall design of the framework and precise regulation at the molecular level simultaneously.[12–14] Furthermore, they often exhibit some attractive and innovative properties compared with precursor units due to the effects of molecular stacking and intermolecular interactions.[15] Both pre-design and post-modification are available. When coupled with their clear and ordered structures, COFs can be easily customized according to actual needs, providing a prevalent material platform for addressing resource,[16,17] environmental,[18] and energy[19] issues. Recently, some COFs used existing ECL emitters as structural components to achieve ECL,[20,21] which is not surprising, and the highly active co-reactants and signal amplifiers are still required. However, activating and using efficient ECL of non-emitting molecules has not been demonstrated, let alone in COFs.

Here, a class of COFs is designed as an ECL luminophore family. Using benzo[1,2-b:3,4-b″:5,6-b″″]trithiophene-2,5,8-tricarbaldehyde (BTT) as key electron donor, a series of crystalline BTT-COFs are synthesized by conjugating different electron receptors through carbon-carbon double bonds (–C=C–). The intramolecular charge transfer (ICT) states, which, generated by the collision between the donor BTT and the electron acceptor, arouses effective ECL emissions, and the enhancement of the electron-withdrawing ability of the acceptors can modulate the ECL by shortening the electron transfer pathway. In an aqueous medium with the inner dissolved oxygen as co-reactant, the tunable ECL of the BTT-COFs can be achieved without any exogenous noxious co-reactants, providing a seminal pathway to obtain ECL from the ECL non-active monomers. Moreover, with the cyano group weaved into the skeleton, the BTT-COFs provided the dense post-functionalization sites for the wider practical applications. For example, as a proof-of-concept sensing application, a superb "turn-on" UO_2^{2+} monitoring system is constituted by introducing the amidoxime (AO) groups in the open channels of BTT-COFs, and the electron transfer of UO_2^{2+} to the COFs skeletons can lead to the further increase in ECL intensity. It is revealed that the combination of ECL and BTT-COFs affords a potent platform for tailor-made detection of various types of pollutants.

RESULTS AND DISCUSSION

Material design considerations of COFs for ECL

To activate efficient ECL from ECL non-active monomers in aqueous medium and establish an original ECL luminophores family, we have the following materials design considerations. With easily controlled charge dynamics, a donor-acceptor (D-A) heterojunction is a pivotal component in varying photoelectric devices and photovoltaic technology.[22–24] COFs provide an attractive platform, in which building blocks can be pre-designed, orderly stacked, and interconnected, and tend to exhibit unexpected innovative properties.[25,26] Therefore, a superb ECL may be achieved by constructing well-organized D-A structures in COFs' skeleton. Although optoelectronic materials based on D-A structures have been fully studied before, it is still a challenge to design and synthesize D-A COFs with ECL performance because the donors and acceptors are more inclined to stack on top of each other randomly rather than separate to form a bicontinuous columnar array, resulting in a disordered assembly and charge carrier annihilation.[27]

Besides the building blocks, the luminescence activity of COFs is also highly dependent on the linkage. The linkages exist in an indispensable position in single-layer

**Cell Reports
Physical Science
Article**

CellPress
OPEN ACCESS

and stacked frames; peeling or stacking of layers can hardly change their role in glowing. In many cases, COF luminescence is quenched by the loss of excitation energy in the process of electron transfer.[28] For instance, the imine-linked and hydrazone-linked COFs, despite using high-efficiency chromophores, still emit poor luminescence due to the connecting nitrogen atoms.[29,30] In this context, the olefin bond provides a promising approach to luminescent COFs by removing the inherent limitation of fluorescence quenching caused by N-linkages, showing beneficial influences on the higher π-conjugation along the skeleton and more efficient π-electron transfer in the COF lattice.

Based on the above considerations, we introduced a strong electron-rich BTT as a core node to provide stable conjugate bonds and high electrical conductivity for charge transfer. Three hexagonal olefin-linked D-A COFs (BTT-COFs) were design and constructed by Knoevenagel polymerization with different acceptor molecules 2,4,6-trimethylbenzene-1,3,5-tricarbonitrile (TBTN), 2,4,6-trimethylpyridine-3,5-dicarbonitrile (DCTP), and 2,4,6-trimethyl-1,3,5-triazine (TMT), respectively (Figure 1A).

Characterizations of BTT-COFs

Under solvothermal conditions, the expected high crystallinity BTT-TBTN, BTT-DCTP, and BTT-TMT were obtained by condensation reaction for 3 days using the optimized catalyst (see supplemental experimental procedures for synthetic procedures and Figures S1−S3 for optimized catalyst). The Fourier transform infrared (FTIR) spectra (Figures S4−S6) and ^{13}C cross-polarization/magic-angle-spinning (CP/MAS) NMR (Figures S7−S9) of BTT-TBTN, BTT-DCTP, and BTT-TMT confirmed the successful formation of olefin linkages in the skeletons.[5,31,32] The crystal structures of BTT-TBTN, BTT-DCTP, and BTT-TMT were further evaluated by powder X-ray diffraction (PXRD), which showed sharp and strong first peaks at 6.81°, 6.81°, and 6.62° (2θ) (Figures 1B–1D), respectively, attributable to the intense reflection from (100) planes, confirming their high crystallinity. In addition, these PXRD patterns agreed well with the eclipsed AA-stacking models (Figures 1B–1D, inset; Tables S1–S3), and the Pawley refined PXRD profiles matched well with the experimental data ($R_{wp} \leq 2.63\%$ and $R_p \leq 2.02\%$), as evidenced by the negligible pattern differences (Figures 1B–1D). The models proposed for the BTT-TBTN (Table S1) and BTT-TMT (Table S3) were in the *P-6* space group, and the BTT-DCTP was in the *PM* space group (Table S2).

The detailed pore characteristics of BTT-TBTN, BTT-DCTP, and BTT-TMT were evaluated by the N_2 adsorption-desorption experiments at 77 K. It was found that some mesoporous existed in BTT-COFs (Figures S10−S12), which may be attributed to the intercrystal porosity formed by the packing of non-uniform crystals and crystal defects.[33] The pore size distributions maximum centered at 1.1, 1.1, and 1.3 nm for BTT-TBTN, BTT-DCTP, and BTT-TMT (Figures S13−S15), respectively, which can agree well with the proposed AA eclipsed models (insets of Figures 1B–1D). Calculated by the Brunauer-Emmett-Teller (BET) model, the specific surface areas of BTT-TBTN, BTT-DCTP, and BTT-TMT were 586.5, 596.6, and 325.2 $m^2 \cdot g^{-1}$ (Figures S16−S18), respectively. The thermogravimetric analysis (TGA) curves showed the BTT-TBTN, BTT-DCTP, and BTT-TMT were thermally stable up to ∼300°C (Figure S19). All of the above results strongly support the successful construction of the high crystallinity olefin-linked BTT-COFs by efficient polycondensation.

Optoelectronic property

Photoelectric experiments were then performed to evaluate and compare the synthesized BTT-COFs. The small semicircular domains in electrochemical impedance
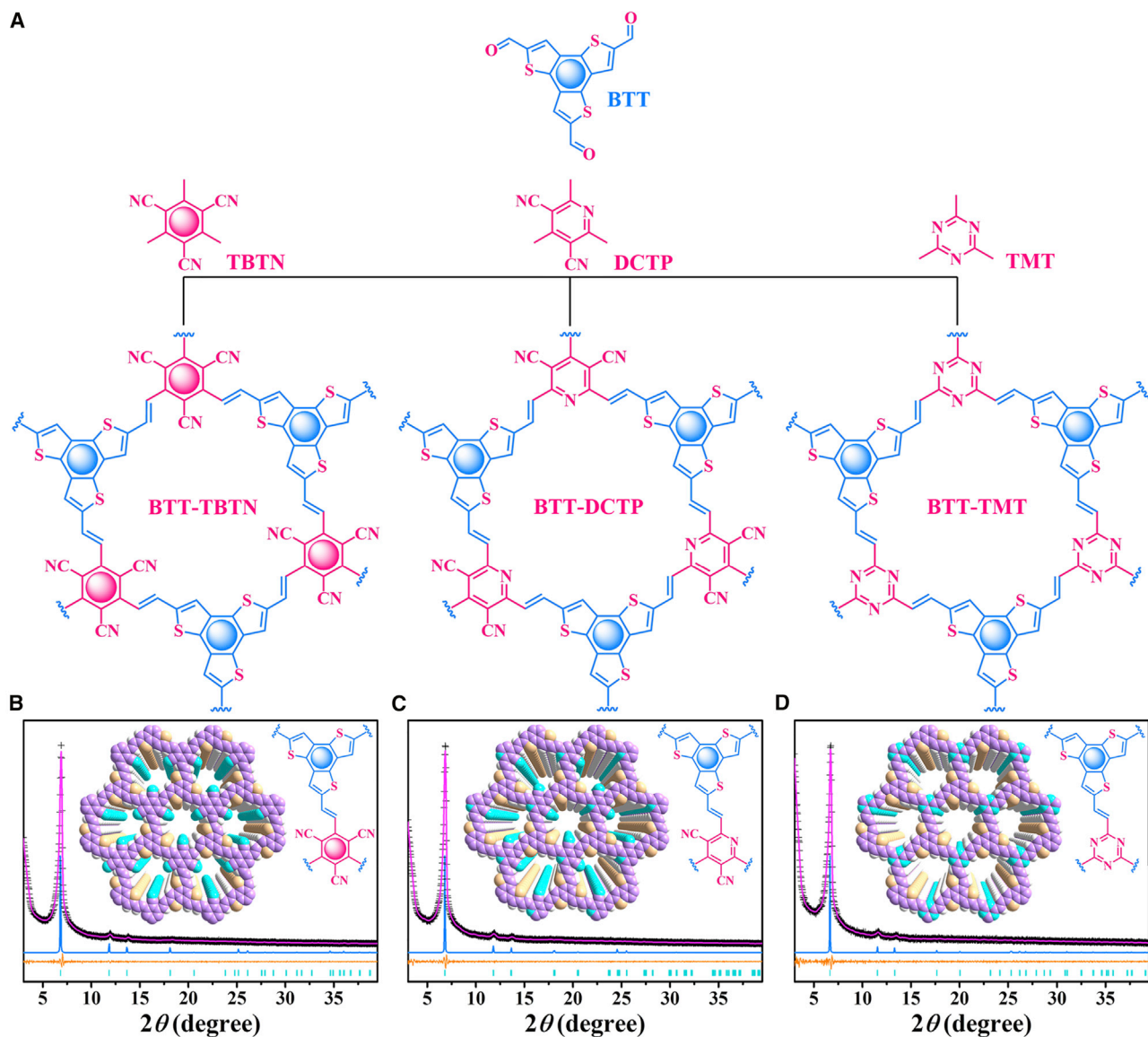
Figure 1. Synthesis and PXRD spectra of D-A fully conjugated BTT-COFs

(A) Schematic diagram for the synthesis of D-A fully conjugated BTT-COFs.

(B–D) PXRD of BTT-TBTN (B), BTT-DCTP (C), and BTT-TMT (D): comparison between the Pawley refined (pink line) and experimental (black cross) profiles, the eclipsed stacking mode (blue line), the Bragg positions (green bar), and the refinement differences (orange line).

Insets of (B–D): Top views of an eclipsed AA-stacking model of BTT-TBTN (B), BTT-DCTP (C), and BTT-TMT (D) (light purple, C; cyan, N; light yellow, S; white, H).

spectroscopy (EIS) showed the relatively small electron transfer resistances (Rets) of the BTT-COFs, of which the smallest arc diameter of BTT-TBTN implied its highest charge transfer rate (Figure 2A).[14] Their transient photocurrent responses were then examined under external bias voltage when irradiated by chopping through several light on/off cycles (Figure 2B). During a 300-s measurement period, all of the BTT-COFs showcased ultra-high photocurrent densities, suggesting effective charge carrier separation. As shown in the UV-visible light (UV-vis) diffuse reflectance spectra (UV-vis DRS), the COFs woven from TBTN had a wider boundary absorption spectrum than those of DCTP and TMT, with a high maximum absorption
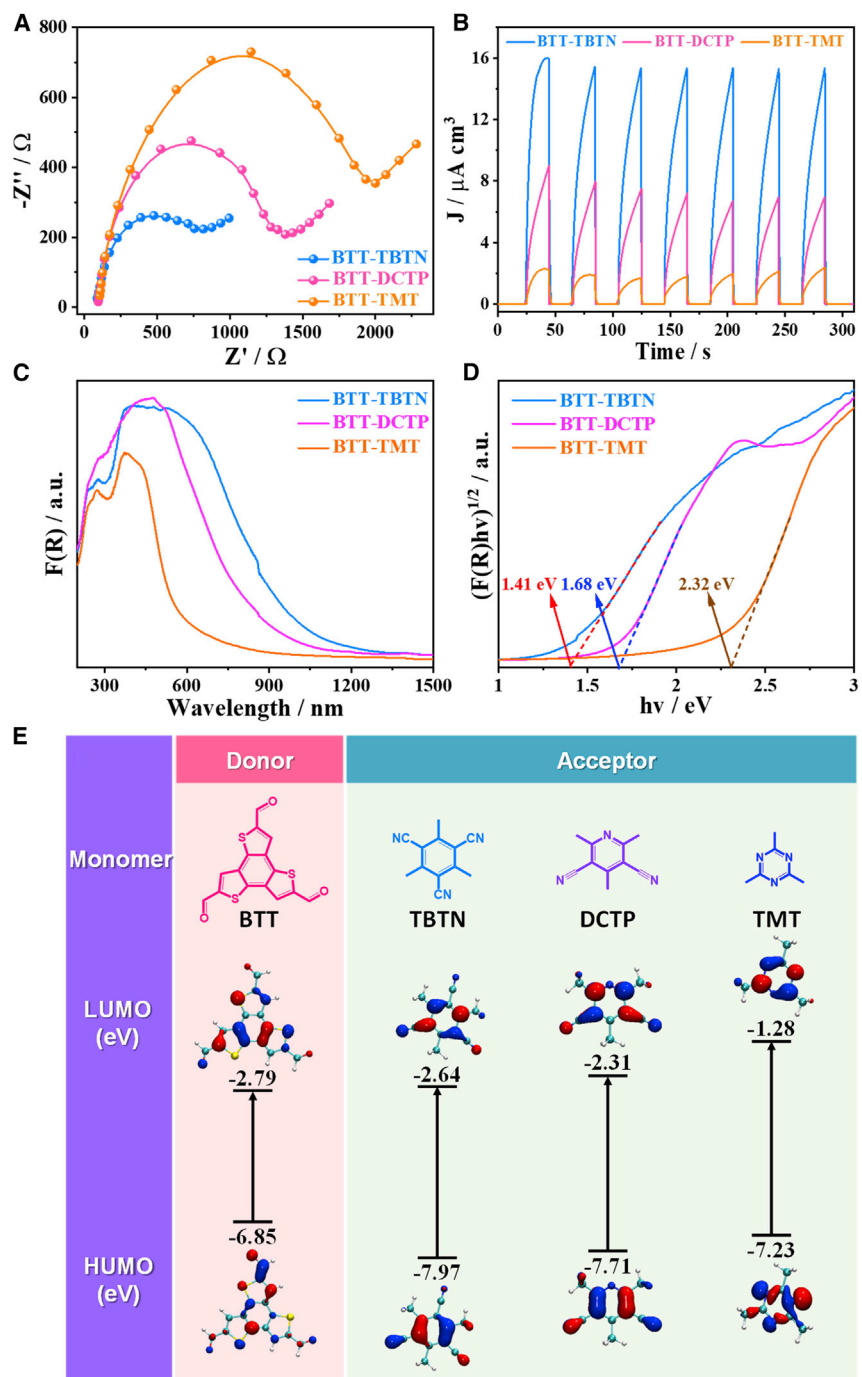
Cell Reports
Physical Science
Article

Figure 2. Optoelectronic properties

(A) Electrochemical impedance spectroscopy curves of BTT-COFs.

(B) Photocurrent responses of BTT-COFs upon visible light irradiation.

(C) UV-visible diffuse reflectance spectra of BTT-COFs.

(D) Kubelka-Munk-transformed reflectance spectra of BTT-COFs.

(E) The HOMO and LUMO distributions and calculated energy gaps of monomer BTT, TBTN, DCTP, and TMT.

wavelength of 1,200 nm, indicating the best light-harvesting capacity of BTT-TBTN (Figure 2C). The optical band gaps of each COF can be further ascertained from the Kubelka-Munk-transform reflection spectrum in the order of BTT-TBTN (1.41 eV) < BTT-DCTP (1.68 eV) < BTT-TMT (2.32 eV) (Figure 2D). It can be comprehended in more depth by the density functional theory (DFT) calculations. The calculated lowest unoccupied molecular orbital (LUMO) of TBTN is lower than those of DCTP and TMT by 0.26 and 0.74 eV, respectively, which means the electron-receiving and electron-transfer are more likely to occur (Figure 2E). The BTT-TBTN, with the strongest D-A structure, evidently increased the photoelectric response and reduced the optical band gap simultaneously.[5]

Hence, through the ordered stacking of olefin-bridged D-A fully conjugated building blocks, BTT-COFs provided an efficient interface charge transfer platform, enabling more electrons and holes to be excited, and demonstrating above gratifying semiconductor activities.

ECL performance

Encouraged by the intriguing photophysical properties and electrochemical behaviors of BTT-COFs, their anticipated ECL performances were explored. The assembly of COFs on the electrode surface was completed by casting 10 μL of 1 mM of the prepared BTT-COFs/DMF solution on the surface of the treated glassy carbon electrode (GCE) and drying at room temperature. After optimizing the cathode and anode scanning potential of BTT-TBTN, the best potential window for the BTT-COFs/GCE ECL systems was found (−2.8 to 0 V) for the following studies (Figure S20). Under the same experimental conditions, however, no significant ECL signals were observed from all the monomers constituting BTT-COFs (Figure S21), eliminating the possible ECL generated by unpredictable interference.

When optimizing the solvent of the ECL system, it was surprising that the BTT-COFs showed a stronger ECL signal in the aqueous phosphate buffer saline (PBS) than in various organic phases (Figure 3A). Although researchers have studied the ECL of many organic substances (e.g., polycyclic aromatic hydrocarbons) in non-proton solvents, few can emit in aqueous solutions, which is attributed to the poor solubility and stability of free radical ions and aggregation-induced quenching by water and oxygen.[4,8] Some typical organic ECL luminophores such as pyrene (Py), perylene (Pe), diphenylanthracene (DPA), rubrene (Rub), 5,10,15,20-tetrakis(4-hydroxy-phenyl)porphyrin (THPP), and boron dipyrromethene (BODIPY), were also tested under the same experimental conditions, showing faint signals (Figure 3B). The enhanced ECL of the BTT-COFs in water can come from the elimination of harmful π-π accumulation and the inhibition of molecular motions, thus blocking non-radiative attenuation channels and being advantageous to the electron flow from the donor BTT to the receptors.

During the 12 repeated-measurement periods, the ECL emission gradually increased in the first 3 electrochemical cycles as the oxidizing intermediates increased, after which, the signals were stable with a relative standard deviation (RSD) of 1.6% (Figure 3C), indicating that the BTT-COFs were stable enough for ECL scanning without damaging the crystal structures. It was also proved that the BTT-TBTN structure remained intact by collecting the BTT-TBTN powder during the 0 to 720 s electrochemical scans and characterizing the structure (Figure S22), which ensures great reproducibility. The advantages endowed BTT-COFs with great potential applications in numerous life-related areas.
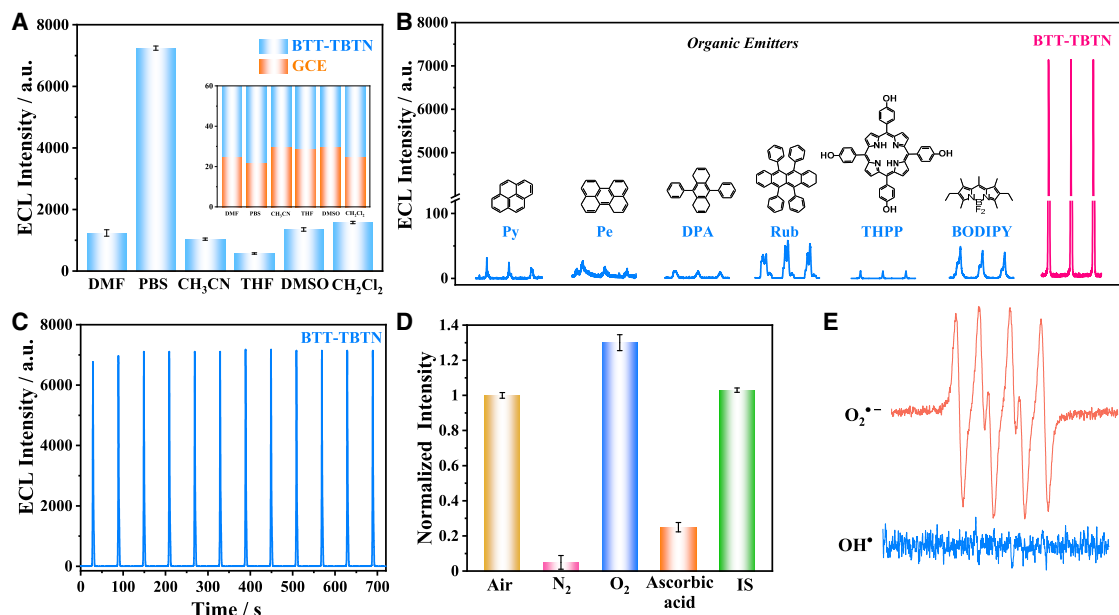
Figure 3. ECL performance

(A) ECL intensity of BTT-TBTN/GCE (blue) and bare GCE (orange) in different solvents. The inset is a local magnification of ECL intensity from 0 to 60 a.u. Error bars represent SD; n = 3 independent experiments.

(B) ECL-time curves of 10 µL 1 mM different organic ECL luminophores (Py, Pe, DPA, Rub, THPP, BODIPY) and BTT-TBTN modified GCE.
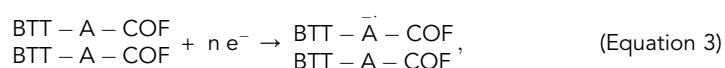
(C) ECL-time curves of BTT-TBTN under the 12 continuous periodic scans.
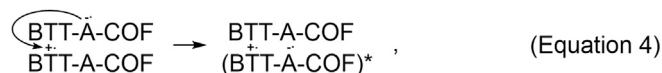
(D) Normalized ECL intensity of BTT-TBTN/GCE within air, N_2-saturated, O_2-saturated, 0.1 mM ascorbic acid, and 0.1 mM IS. Error bars represent SDs; n = 3 independent experiments. All of the buffer solutions throughout the ECL experiments were 0.1 M PBS with 0.1 M KCl between 0 and −2.8 V, pH 7.5, the photomultiplier tube (PMT): 800 V; potential scan rate: 100 mV s^{-1}.

(E) EPR spectra of BTT-TBTN.

To clarify the ECL mechanism of BTT-COFs, the effects of different atmosphere conditions and free-radical scavengers on the ECL intensity of BTT-TBTN were investigated to determine the active intermediates in the BTT-COFs-ECL systems. As illustrated in Figure 3D, a weak ECL signal was found in the N_2-saturated PBS solution (reduced by 95%), but the signal increased by 1.3 times in an O_2-saturated system, which manifested the key role of dissolved oxygen. The addition of 1.0 mM isopropanol (IS), as a hydroxyl radical (OH·) scavenger,[34] had no effect on the ECL, while the superoxide anion scavenger ($O_2^{-\cdot}$), ascorbic acid,[35] significantly quenched the ECL intensity by 75%, which was also identified by the electron paramagnetic resonance (EPR) measurement (Figure 3E), confirming that the ECL reaction was through an $O_2^{-\cdot}$-dominated free radical pathway. The high superficial area and abundant pores of BTT-COFs here provided places for O_2 free diffusion and guaranteed rapid interactions with $O_2^{-\cdot}$, which was conducive to achieving the stable ECL emission quickly.

According to the above discussion, the ECL formation mechanism of BTT-COFs is proposed as in Equations 1, 2, 3, 4, and 5:

$$O_2 + e^- \rightarrow O_2^{-\cdot}, \qquad \text{(Equation 1)}$$

$$\begin{matrix} BTT-A-COF \\ BTT-A-COF \end{matrix} + O_2^{-\cdot} \rightarrow \begin{matrix} BTT-A-COF^{+\cdot} \\ BTT \end{matrix}-A-COF+O_2^{2-}, \qquad \text{(Equation 2)}$$

$$\begin{matrix} BTT-A-COF \\ BTT-A-COF \end{matrix} + n\,e^- \rightarrow \begin{matrix} BTT-\bar{A}-COF \\ BTT-A-COF \end{matrix}, \qquad \text{(Equation 3)}$$

$$\begin{array}{c} \text{BTT-A-COF} \\ \text{BTT-A-COF} \end{array} \longrightarrow \begin{array}{c} \text{BTT-A-COF} \\ (\text{BTT-A-COF})^* \end{array} , \qquad \text{(Equation 4)}$$

and

$$(BT^{+\cdot}T - A^{-\cdot} - COF)^* \overset{ICT}{\to} BTT - A - COF + hv. \qquad \text{(Equation 5)}$$

At the cathode, O_2 pioneered the electrochemical reduction and generated the oxidizing intermediate ($O_2^{-\cdot}$) (Equation 1). The hole was then injected into the highest occupied molecular orbital (HOMO), which was located at the vertex BTT. The extended π-electron communication of BTT-COFs effectively promoted the hole transmission and further produced the cationic radicals (Equation 2). In the same electrochemical scanning, the electrons continued to flow into the LUMOs, which were distributed on the acceptor units ("A" represents the TBTN, DCTP, and TMT), until the anion radicals of BTT-COFs were obtained near the reduction potential (Equation 3). The free radical ions collided with one another to form the ICT states directly (Equation 4), and finally returned to the ground state upon a strong ECL emission (Equation 5).

ECL regulated by the electron-withdrawing units

The inherent advantages of the precise design of COFs prompted us to explore the tunable ECL. A series of BTT-COFs were subsequently constructed by attaching different electron-withdrawing monomers (Figure 1A). The differentiated cathodic enhanced ECL emissions of BTT-COFs were observed in 0.1 M PBS, which were 248.9, 212.8, and 6.1 times (for BTT-TBTN, BTT-DCTP, and BTT-TMT) higher than that of the GCE, respectively (Figures 4A–4C). The cyclic voltammetry (CV) curves showed obvious reduction waves of BTT-COFs, corresponding to the ECL initial potential of −2.5, −2.3, and −1.8 V, indicating that the electron injection process started the ECL production (Figures 4D–4F). Remarkably, the calculated ECL efficiencies of BTT-TBTN and BTT-DCTP in aqueous media were up to 62.2% and 53.2%, respectively, despite no distinct signals occurring in all of the related monomers (Figure S21) and the absence of exogenous high-oxidizing co-reactants.

To gain more insight into the tunable ECL phenomenon and unravel the plausible reason for the better performance of BTT-TBTN over others, a building block of each BTT-COF was extracted as a model and we performed DFT calculations. It can be seen that the HOMOs are concentrated on the π-conjugated main chain of electron-donor BTT, while the LUMOs are located on the electron-acceptors TBTN, DCTP, and TMT, elucidating that the HOMO-LUMO transition between BTT and TBTN/DCTP/TMT is an intramolecular charge transfer transition, similar to some ECL emitters involving donor-receptor pairs.[27,36–42] When excited, electrons and holes effectively separated, and the molecular orbitals' overlap greatly reduced (Figure S23). The flow of electrons from BTT to electron-withdrawing units can take place within the extended skeletons of BTT-COFs. The theoretical HOMO-LUMO band gaps followed the order of BTT-TBTN < BTT-DCTP < BTT-TMT (Figure S23). The enhancement of the electron deficiency in COF skeletons significantly reduces the band gap by shortening the electron transition distance from the valence electrons to the conduction band, which makes it easier to obtain the excited state along the ECL route.[43,44] It is also noted that when the synthesized materials grow to the extended π-conjugate planes from the single building blocks,
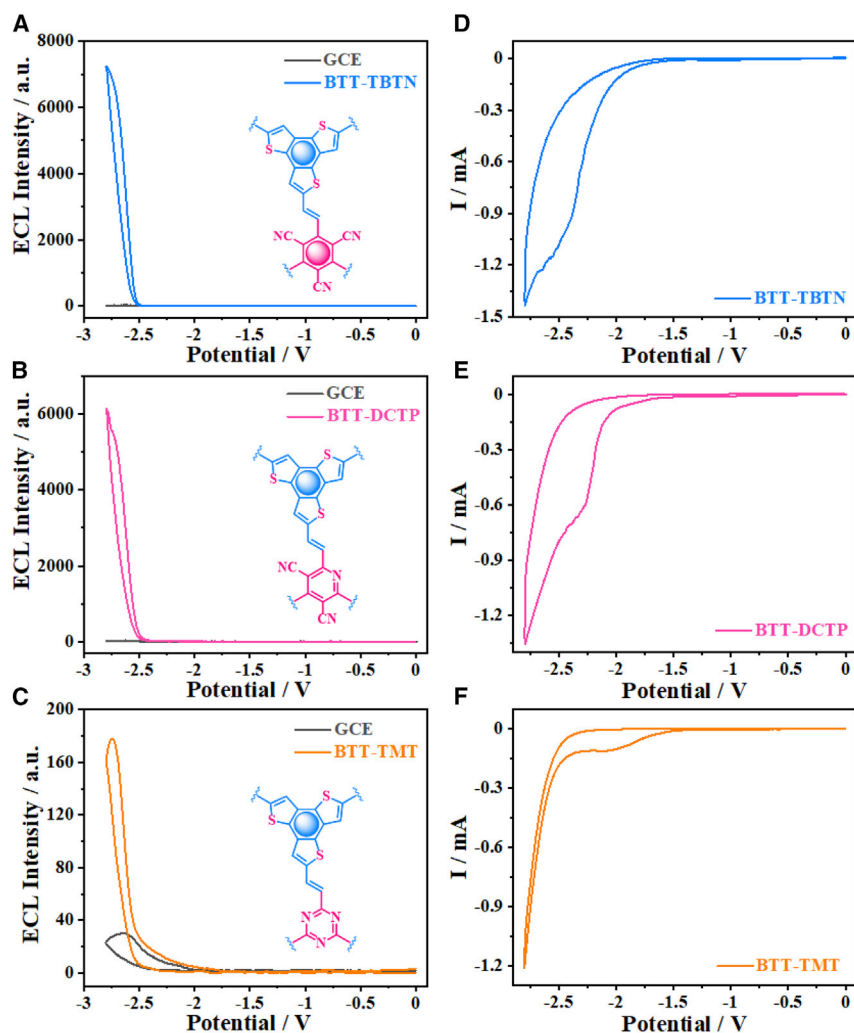
Figure 4. Comparison of BTT-COFs with different acceptors

(A–C) The ECL-potential curves of BTT-TBTN (A), BTT-DCTP (B), and BTT-TMT (C).

(D–F) The CV curves of BTT-TBTN (D), BTT-DCTP (E), and BTT-TMT (F) modified GCE in 0.1 M PBS (pH 7.5) with a potential range of $-2.8\sim0$ V; scan rate: 100 mV s^{-1}, PMT = 800 V.

the band gaps are greatly reduced by 1.09–1.46 eV, owing to the freer electron transfer and the smoother π-electron communication (Figure 2D).

The above-mentioned theoretical results agreed well with our conception. By confining the donor BTT and electron pulling monomer to the ordered olefin-linked electron configuration of the BTT-COFs, the charge transfer could conduct efficiently and reach an ECL emission. Moreover, the adjustable electron deficiency, which results from the differentiated electron transfer and transition, makes the stronger electron-withdrawing molecule generate the more effective ECL emission by reducing the energy gap. Thus, the ECL manifestation can be changed easily by changing the D-A component of COFs alone, facilitating dynamic designs tailored for practical applications.

Compared to the AIE-gens, the BTT-COFs designed here possess the advantages of simple synthesis, clear structure, orderly stacking, and high stability. The ECL
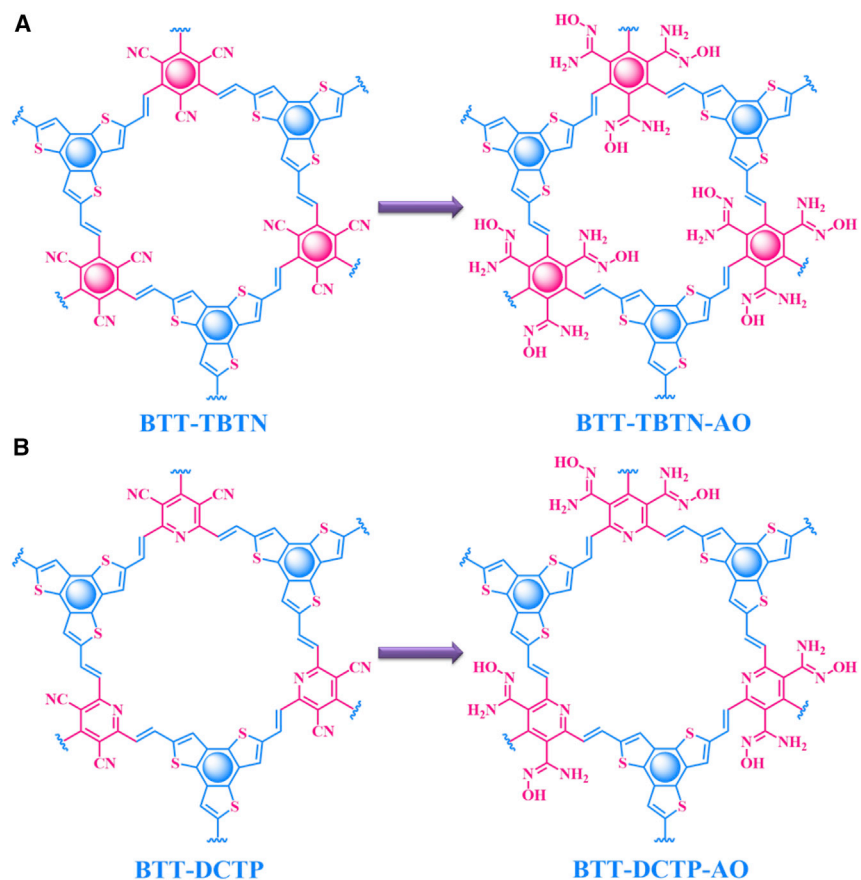
Cell Reports
Physical Science
Article

Figure 5. Schematic diagram
(A and B) The synthesis of BTT-TBTN-AO (A) and BTT-DCTP-AO (B).

emission can be produced in various solvents, and the highest efficiency is achieved in water even without any co-reaction. BTT-COFs can be further developed into a variety of multi-functional materials with specific sensing capacities, and we also expect them to be the potent platforms for promoting the exploration of structure-performance mechanisms.

Sensitive detection of uranyl ions

Based on the excellent spatial and temporal control of ECL and the outstanding versatility of COFs, the synthesized BTT-COFs provided a potent platform for tailor-made detection of various types of pollutants. As a proof-of-concept sensing application, a UO_2^{2+} sensing platform was further developed to deal with the major environmental problems caused by industrial pollution related to nuclear energy.

In our design, the pre-weaved cyano groups within the BTT-TBTN and BTT-DCTP can further evolve into the dense AO groups as powerful tentacles for capturing UO_2^{2+} specifically. As a preferred UO_2^{2+} chelating group, the AO group is easy to react with the building units and inhibits the formation of COFs; a two-step synthesis was adopted here.[32] After swelling in absolute ethanol, the crystalline BTT-TBTN and BTT-DCTP were treated with excess $NH_2OH \cdot HCl$ and triethylamine at 85°C for 24 h, obtaining the BTT-TBTN-AO and BTT-DCTP-AO (Figures 5A and 5B). The characterizations of BTT-TBTTN-AO and BTT-DCTP-AO are described in Figures S24–S37.
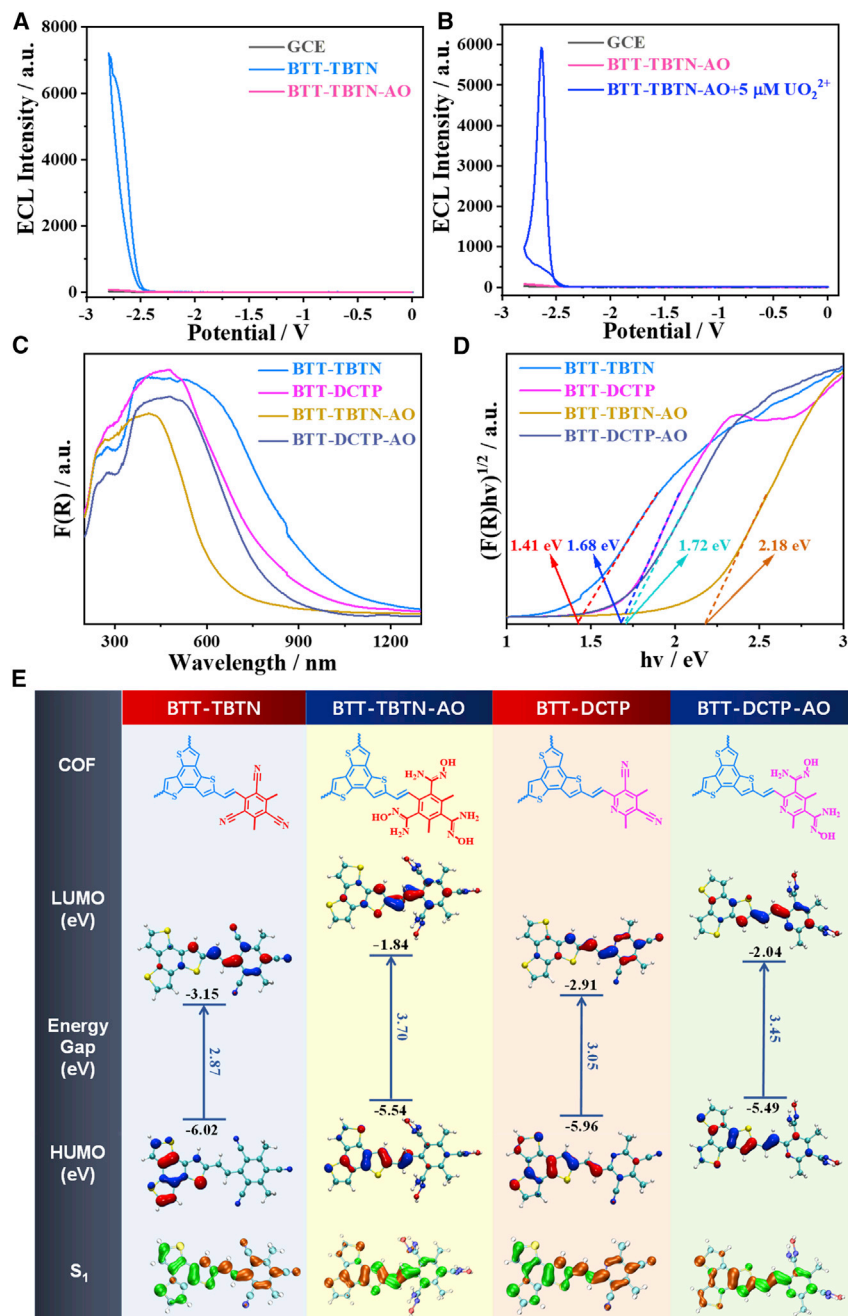
Cell Reports
Physical Science
Article

Figure 6. Uranyl ion detection mechanism

(A) The ECL-potential curves of GCE, BTT-TBTN, and BTT-TBTN-AO.

(B) The ECL-potential curves of GCE, BTT-TBTN-AO, and BTT-TBTN-AO with 5 μM UO_2^{2+}.

(C) UV-visible diffuse reflectance spectra of BTT-COFs and BTT-COFs-AO.

(D) Kubelka-Munk-transformed reflectance spectra of BTT-COFs and BTT-COFs-AO.

(E) The comparison of HOMO/LUMO distributions, calculated energy gaps, and the S_1 analysis (green represents hole and orange represents electron) of BTT-COFs.

Then, in a typical case, 10 μL of 1 mM BTT-TBTN-AO/DMF solution was coated on a GCE and dried to obtain the ECL sensor BTT-TBTN-AO/GCE. Under the same experimental conditions, the ECL signal of BTT-TBTN-AO was almost completely quenched, accompanied by a blue shift of the UV absorption boundary
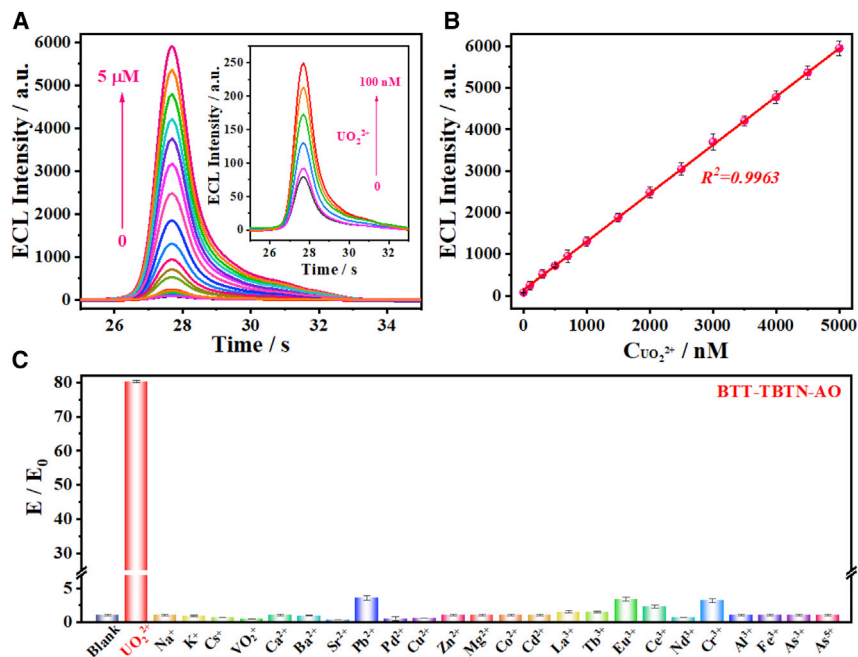
Figure 7. Trace UO_2^{2+} monitoring
(A) ECL-time curves of BTT-TBTN-AO with UO_2^{2+} from 0 to 5 μM. Inset: ECL-time curves of BTT-TBTN-AO with UO_2^{2+} from 0.01 to 100 nM.
(B) The calibration curve of ECL intensity versus UO_2^{2+} concentration.
(C) The selective detection of the test cations. Error bars represent SDs; n = 3 independent experiments.

(Figures 6A and 6C). This can be attributed to the destruction of the ordered D-A structure and the increase in the band gaps, as well as a decrease in the separation of electrons and holes (Figures 6D and 6E). The Nyquist curves of the BTT-TBTN-AO and BTT-DCTP-AO showed the semicircles with larger diameters compared to BTT-COFs, indicating the decreased interfacial charge transfer rate (Figure S38). At this point, the ICT states became unavailable. Surprisingly, under the near-zero background signal provided by BTT-TBTN-AO, the signal was enhanced by 80.3 times upon adding 5 μM UO_2^{2+} (Figure 6B). The generality was proved by the BTT-DCTP, another favorable ECL luminophore designed in this work. Using the same method, a UO_2^{2+} detection platform BTT-DCTP-AO/GCE/PBS was built. Similarly, under the ultra-low background signal of BTT-DCTP-AO/GCE/PBS, 5 μM UO_2^{2+} can enhance the ECL of the system by 21.3 times (Figure S39). UO_2^{2+} has very little cathode ECL (even lower than the GCE in PBS; Figure S40) and has no effect on the ECL of undecorated BTT-TBTN (Figure S41), which guides us to a deeper exploration.

To establish the optimal detection conditions, quite a few controlled experiments of pH and incubation time were performed (Figure S42). Then, the ECL signal related to the UO_2^{2+} concentration was measured after incubating the BTT-TBTN-AO/GCE sensor with 300 μL standard UO_2^{2+}/PBS solution (pH 5.5) for 5 min (Figure S42). With the increase in UO_2^{2+} concentration from 0.01 nM to 5 μM, the ECL of BTT-TBTN-AO-UO_2^{2+} was gradually enhanced (Figure 7A). The relationship between ECL intensity and logarithm of UO_2^{2+} concentration was linear, providing a limit of detection (LOD) of 3.5 pM or 0.82 ppt (Figure 7B). The superiority of this UO_2^{2+} sensing probe in the high sensitivity is well reflected by the ultra-low LOD, which

CellPress
OPEN ACCESS

is 2 orders of magnitude lower than the reported luminous UO_2^{2+} probe and lower than the other reported ECL probe modified with ssDNA (Table S4). For the BTT-DCTP-AO/GCE/PBS, another constructed UO_2^{2+} monitoring platform, a good linear relationship was also seen with a LOD of 23.2 pM/5.47 ppt (Figure S43), which was much lower than the World Health Organization (WHO) UO_2^{2+} pollution limit in drinking water (63 nM). Since the TBTN monomer had one less cyano group on DCTP, it provided fewer chelating sites, and the sensitivity of BTT-DCTP-AO/GCE/PBS to UO_2^{2+} response was correspondingly decreased.

The selectivity of these two UO_2^{2+} probes was verified by comparing some cations and anions, which may interfere with it in seawater (Figures 7C and S44). Even with 50 μM, these ions, 10 times those of UO_2^{2+}, still had no obvious enhancement in the ECL signals, which can originate from the specific affinity of the open channel AO group to UO_2^{2+} in BTT-TBTN-AO. The interaction with UO_2^{2+} was then traced using X-ray photoelectron spectroscopy (XPS). As depicted in Figure S45, 2 characteristic peaks for U 4f appeared (393.9 eV for U $4f^{5/2}$ and 382.5 eV for U $4f^{7/2}$), indicating the UO_2^{2+} loading onto the BTT-TBTN-AO after the ECL process.[32] In the N_1 high-resolution XPS spectrum of BTT-TBTN-AO, the N-containing C–N and C=N corresponded to the 2 binding energy peaks of 400.0 and 398.9 eV, respectively.[32] After finishing the UO_2^{2+} detection, forming a new N-U peak at 401.2 eV, the peaks at 398.9 eV moved 0.2 eV toward the higher binding energy. No shift in the peak located at 400.0 eV was observed, suggesting that the N atoms in C=N cannot combine with UO_2^{2+} (Figures S46A and S46B). Similarly, a new O-U peak (531.3 eV) was observed in the O 1 s spectrum, and the C=N-OH of BTT-TBTN-AO shifted 0.4 eV to a higher binding energy (Figures S46C and S46D). However, the binding energy of the S 2 s did not change before and after the reaction (Figure S47), demonstrating that the S do not become involved in the coordination. Accordingly, it can be inferred that the AO groups in BTT-TBTN-AO participated in the UO_2^{2+} coordination (Figure S48), like the previously reported binding modes.[32,45–48] The UO_2^{2+} detection mechanism using AO groups as chelating sites is proposed to proceed as Figure S49. The UO_2^{2+} plays the core role of electrocatalytic redox reaction, and its morphology remains unchanged before and after the reaction, ensuring the stability and reproducibility of the detection.

To confirm the practicability of the probes in actual samples, the seawater/freshwater samples of the South China Sea, the East China Sea, the Yangtze River, and Poyang Lake were collected to measure the UO_2^{2+} concentrations (Table S5). The measured results were consistent with the inductively coupled plasma-mass spectrometry (ICP-MS), implicating the valued application prospect in the field of environmental analysis.

EXPERIMENTAL PROCEDURES
Resource availability
Lead contact
Further information and requests for resources should be directed to and will be fulfilled by the lead contact, Jian-Ding Qiu (jdqiu@ncu.edu.cn).

Materials availability
The full details of all materials are provided in the supplemental information.

Data and code availability
All data are either provided in the article and supplemental information or are available from the lead contact upon request.

CellPress
OPEN ACCESS

Cell Reports
Physical Science
Article

SUPPLEMENTAL INFORMATION

ACKNOWLEDGMENTS

AUTHOR CONTRIBUTIONS

Conceptualization, J.-D.Q. and R.-P.L.; investigation, Y.-J.L. and W.-R.C.; methodology, Q.-Q.J., Q.W., and Q.-X.L.; writing – original draft and review & editing, Y.-J.L., W.-R.C., J.L., R.-P.L., and J.-D.Q.; supervision, funding acquisition, and project administration, J.-D.Q., R.-P.L., and L.Z.

DECLARATION OF INTERESTS

The authors declare no competing interests.

REFERENCES

1. Fiorani, A., Valenti, G., Iurlo, M., Marcaccio, M., and Paolucci, F. (2018). Electrogenerated chemiluminescence: A molecular electrochemistry point of view. Curr. Opin. Electrochem. *8*, 31–38.

2. Qi, H., and Zhang, C. (2020). Electrogenerated chemiluminescence biosensing. Anal. Chem. *92*, 524–534.

3. Lv, Y., Chen, S., Shen, Y., Ji, J., Zhou, Q., Liu, S., and Zhang, Y. (2018). Competitive multiple-mechanism-driven electrochemiluminescent detection of 8-hydroxy-2′-deoxyguanosine. J. Am. Chem. Soc. *140*, 2801–2804.

4. Wei, X., Zhu, M.J., Yan, H., Lu, C., and Xu, J.-J. (2019). Recent advances in aggregation-induced electrochemiluminescence. Chemistry *25*, 12671–12683.

5. Cui, L., Yu, S., Gao, W., Zhang, X., Deng, S., and Zhang, C.Y. (2020). Tetraphenylenthene-based conjugated microporous polymer for aggregation-induced electrochemiluminescence. ACS Appl. Mater. Interfaces *12*, 7966–7973.

6. Han, Z., Zhang, Y., Wu, Y., Li, Z., Bai, L., Huo, S., and Lu, X. (2019). Substituent-induced aggregated state electrochemiluminescence of tetraphenylethene derivatives. Anal. Chem. *91*, 8676–8682.

7. Ji, S.-Y., Zhao, W., Gao, H., Pan, J.-B., Xu, C.-H., Quan, Y.-W., Xu, J.-J., and Chen, H.-Y. (2020). Highly efficient aggregation-induced electrochemiluminescence of polyfluorene derivative nanoparticles containing tetraphenylethylene. iScience *23*, 100774.

8. Han, Z., Yang, Z., Sun, H., Xu, Y., Ma, X., Shan, D., Chen, J., Huo, S., Zhang, Z., Du, P., and Lu, X. (2019). Electrochemiluminescence platforms based on small water-insoluble organic molecules for ultrasensitive aqueous-phase detection. Angew. Chem. Int. Ed. Engl. *58*, 5915–5919.

9. Zhao, Z., He, B., and Tang, B.Z. (2015). Aggregation-induced emission of siloles. Chem. Sci. (Camb.) *6*, 5347–5365.

10. Han, T., Feng, X., Shi, J., Tong, B., Dong, Y., Lam, J.W.Y., Dong, Y., and Tang, B.Z. (2013). DMF-induced emission of an aryl-substituted pyrrole derivative: a solid thermo-responsive material to detect temperature in a specific range. J. Mater. Chem. C Mater. Opt. Electron. Devices *1*, 7534–7539.

11. Han, Z., Shu, J., Jiang, Q., and Cui, H. (2018). Coreactant-free and label-free eletrochemiluminescence immunosensor for copeptin based on luminescent immuno-gold nanoassemblies. Anal. Chem. *90*, 6064–6070.

12. Chen, X., Geng, K., Liu, R., Tan, K.T., Gong, Y., Li, Z., Tao, S., Jiang, Q., and Jiang, D. (2020). Covalent organic frameworks: chemical approaches to designer structures and built-in functions. Angew. Chem. Int. Ed. Engl. *59*, 5050–5091.

13. Zhao, X., Pachfule, P., and Thomas, A. (2021). Covalent organic frameworks (COFs) for electrochemical applications. Chem. Soc. Rev. *50*, 6871–6913.

14. Cui, W.-R., Zhang, C.-R., Xu, R.-H., Chen, X.-R., Jiang, W., Li, Y.-J., Liang, R.-P., Zhang, L., and Qiu, J.-D. (2021). Rational design of covalent organic frameworks as a groundbreaking uranium capture platform through three synergistic mechanisms. Appl. Catal. B *294*, 120250.

15. Zeng, J.-Y., Wang, X.-S., and Zhang, X.-Z. (2020). Research progress in covalent organic frameworks for photoluminescent materials. Chemistry *26*, 16568–16581.

16. Wang, H., Wang, H., Wang, Z., Tang, L., Zeng, G., Xu, P., Chen, M., Xiong, T., Zhou, C., Li, X., et al. (2020). Covalent organic framework photocatalysts: structures and applications. Chem. Soc. Rev. *49*, 4135–4165.

17. Lin, S., Diercks, C.S., Zhang, Y.-B., Kornienko, N., Nichols, E.M., Zhao, Y., Paris, A.R., Kim, D., Yang, P., Yaghi, O.M., and Chang, C.J. (2015). Covalent organic frameworks comprising cobalt porphyrins for catalytic CO_2 reduction in water. Science *349*, 1208–1213.

18. Wang, J., and Zhuang, S. (2019). Covalent organic frameworks (COFs) for environmental applications. Coord. Chem. Rev. *400*, 213046.

19. Liu, J., Song, X., Zhang, T., Liu, S., Wen, H., and Chen, L. (2021). 2D conductive metal-organic frameworks: an emerging platform for electrochemical energy storage. Angew. Chem. Int. Ed. Engl. *60*, 5612–5624.

20. Li, S., Ma, X., Pang, C., Wang, M., Yin, G., Xu, Z., Li, J., and Luo, J. (2021). Novel chloramphenicol sensor based on aggregation-induced electrochemiluminescence and nanozyme amplification. Biosens. Bioelectron. *176*, 112944.

21. Zhang, J.-L., Yang, Y., Liang, W.-B., Yao, L.-Y., Yuan, R., and Xiao, D.-R. (2021). Highly stable covalent organic framework nanosheets as a new generation of electrochemiluminescence emitters for ultrasensitive microRNA detection. Anal. Chem. *93*, 3258–3265.

22. Jin, S., Ding, X., Feng, X., Supur, M., Furukawa, K., Takahashi, S., Addicoat, M., El-Khouly, M.E.,

**Cell Reports
Physical Science
Article**

CellPress
OPEN ACCESS

Nakamura, T., Irle, S., et al. (2013). Charge dynamics in a donor-acceptor covalent organic framework with periodically ordered bicontinuous heterojunctions. Angew. Chem. Int. Ed. Engl. *52*, 2017–2021.

23. Rao, J., Yang, L., Li, X., Zhao, L., Wang, S., Ding, J., and Wang, L. (2020). Meta junction promoting efficient thermally activated delayed fluorescence in donor-acceptor conjugated polymers. Angew. Chem. Int. Ed. Engl. *59*, 17903–17909.

24. Izumi, S., Higginbotham, H.F., Nyga, A., Stachelek, P., Tohnai, N., Silva, P., Data, P., Takeda, Y., and Minakata, S. (2020). Thermally activated delayed fluorescent donor-acceptor-donor-acceptor π-conjugated macrocycle for organic light-emitting diodes. J. Am. Chem. Soc. *142*, 1482–1491.

25. Feng, X., Chen, L., Honsho, Y., Saengsawang, O., Liu, L., Wang, L., Saeki, A., Irle, S., Seki, S., Dong, Y., and Jiang, D. (2012). An ambipolar conducting covalent organic framework with self-sorted and periodic electron donor-acceptor ordering. Adv. Mater. *24*, 3026–3031.

26. Xu, S., Sun, H., Addicoat, M., Biswal, B.P., He, F., Park, S., Paasch, S., Zhang, T., Sheng, W., Brunner, E., et al. (2021). Thiophene-bridged donor-acceptor sp^2-carbon-linked 2D conjugated polymers as photocathodes for water reduction. Adv. Mater. *33*, 2006274.

27. Tang, X., Cui, L.-S., Li, H.-C., Gillett, A.J., Auras, F., Qu, Y.-K., Zhong, C., Jones, S.T.E., Jiang, Z.-Q., Friend, R.H., and Liao, L.-S. (2020). Highly efficient luminescence from space-confined charge-transfer emitters. Nat. Mater. *19*, 1332–1338.

28. Li, Z., Huang, N., Lee, K.H., Feng, Y., Tao, S., Jiang, Q., Nagao, Y., Irle, S., and Jiang, D. (2018). Light-emitting covalent organic frameworks: fluorescence improving via pinpoint surgery and selective switch-on sensing of anions. J. Am. Chem. Soc. *140*, 12374–12377.

29. Li, X., Gao, Q., Wang, J., Chen, Y., Chen, Z.-H., Xu, H.S., Tang, W., Leng, K., Ning, G.-H., Wu, J., et al. (2018). Tuneable near white-emissive two-dimensional covalent organic frameworks. Nat. Commun. *9*, 2335.

30. Li, Z., Zhang, Y., Xia, H., Mu, Y., and Liu, X. (2016). A robust and luminescent covalent organic framework as a highly sensitive and selective sensor for the detection of Cu^{2+} ions. Chem. Commun. (Camb.) *52*, 6613–6616.

31. Cui, W.-R., Zhang, C.-R., Xu, R.-H., Chen, X.-R., Yan, R.-H., Jiang, W., Liang, R.-P., and Qiu, J.-D.

(2021). High-efficiency photoenhanced extraction of uranium from natural seawater by olefin-linked covalent organic frameworks. ACS EST Water *1*, 440–448.

32. Cui, W.-R., Li, F.-F., Xu, R.-H., Zhang, C.-R., Chen, X.-R., Yan, R.-H., Liang, R.-P., and Qiu, J.-D. (2020). Regenerable covalent organic frameworks for photo-enhanced uranium adsorption from seawater. Angew. Chem. Int. Ed. Engl. *59*, 17684–17690.

33. Huang, Y.-G., Shiota, Y., Wu, M.-Y., Su, S.-Q., Yao, Z.-S., Kang, S., Kanegawa, S., Li, G.-L., Wu, S.-Q., Kamachi, T., et al. (2016). Superior thermoelasticity and shape-memory nanopores in a porous supramolecular organic framework. Nat. Commun. *7*, 11564.

34. Cao, S.-P., Luo, Q.-X., Li, Y.-J., Liang, R.-P., and Qiu, J.-D. (2020). Gold nanoparticles decorated carbon nitride nanosheets as a coreactant regulate the conversion of the dual-potential electrochemiluminescence of $Ru(bpy)_3^{2+}$ for Hg^{2+} detection. Chem. Commun. (Camb.) *56*, 5625–5628.

35. Saqib, M., Bashir, S., Li, H., Li, C., Wang, S., and Jin, Y. (2019). Efficient electrogenerated chemiluminescence of tris(2,2′-bipyridine) ruthenium(II) with n-hydroxysulfosuccinimide as a coreactant for selective and sensitive detection of l-proline and mercury(II). Anal. Chem. *91*, 12517–12524.

36. Yu, H., Song, X., Xie, N., Wang, J., Li, C., and Wang, Y. (2021). Reversible crystal-to-crystal phase transitions with high-contrast luminescent alterations for a thermally activated delayed fluorescence emitter. Adv. Funct. Mater. *31*, 2007511.

37. Feng, Y., Dai, C., Lei, J., Ju, H., and Cheng, Y. (2016). Silole-containing polymer nanodot: an aqueous low-potential electrochemiluminescence emitter for biosensing. Anal. Chem. *88*, 845–850.

38. Wang, Z., Feng, Y., Wang, N., Cheng, Y., Quan, Y., and Ju, H. (2018). Donor-acceptor conjugated polymer dots for tunable electrochemiluminescence activated by aggregation-induced emission-active moieties. J. Phys. Chem. Lett. *9*, 5296–5302.

39. Feng, Y., Wang, N., and Ju, H. (2018). Highly efficient electrochemiluminescence of cyanovinylene-contained polymer dots in aqueous medium and its application in imaging analysis. Anal. Chem. *90*, 1202–1208.

40. Wang, N., Wang, Z., Chen, L., Chen, W., Quan, Y., Cheng, Y., and Ju, H. (2019). Dual resonance energy transfer in triple-component polymer

dots to enhance electrochemiluminescence for highly sensitive bioanalysis. Chem. Sci. (Camb.) *10*, 6815–6820.

41. Wang, N., Gao, H., Li, Y., Li, G., Chen, W., Jin, Z., Lei, J., Wei, Q., and Ju, H. (2021). Dual intramolecular electron transfer for in situ coreactant-embedded electrochemiluminescence microimaging of membrane protein. Angew. Chem. Int. Ed. Engl. *60*, 197–201.

42. Wang, N., Chen, L., Chen, W., and Ju, H. (2021). Potential- and color-resolved electrochemiluminescence of polymer dots for array imaging of multiplex MicroRNAs. Anal. Chem. *93*, 5327–5333.

43. Li, X., Gao, Q., Aneesh, J., Xu, H.-S., Chen, Z., Tang, W., Liu, C., Shi, X., Adarsh, K.V., Lu, Y., and Loh, K.P. (2018). Molecular engineering of bandgaps in covalent organic frameworks. Chem. Mater. *30*, 5743–5749.

44. Xu, Y., Li, C., Li, Z., Wang, Q., Cai, X., Wei, J., and Wang, Y. (2020). Constructing charge-transfer excited states based on frontier molecular orbital engineering: narrowband green electroluminescence with high color purity and efficiency. Angew. Chem. Int. Ed. Engl. *59*, 17442–17446.

45. Sun, Q., Aguila, B., Earl, L.D., Abney, C.W., Wojtas, L., Thallapally, P.K., et al. (2018). Covalent organic frameworks as a decorating platform for utilization and affinity enhancement of chelating sites for radionuclide sequestration. Adv. Mater. *30*, 1705479.

46. Cui, W.-R., Zhang, C.-R., Jiang, W., Li, F.-F., Liang, R.-P., Liu, J., and Qiu, J.-D. (2020). Regenerable and stable sp^2 carbon-conjugated covalent organic frameworks for selective detection and extraction of uranium. Nat. Commun. *11*, 436.

47. Wu, Y.-D., Cui, W.-R., Zhang, C.-R., Liang, R.-P., and Qiu, J.-D. (2021). Regenerable, anti-biofouling covalent organic frameworks for monitoring and extraction of uranium from seawater. Environ. Chem. Lett. *19*, 1847–1856.

48. Zhang, C.-R., Cui, W.-R., Xu, R.-H., Chen, X.-R., Jiang, W., Wu, Y.-D., Yan, R.-H., Liang, R.-P., and Qiu, J.-D. (2021). Alkynyl-based sp^2 carbon-conjugated covalent organic frameworks with enhanced uranium extraction from seawater by photoinduced multiple effects. CCS Chem. *3*, 168–179.